

FluoCLIP: Stain-Aware Focus Quality Assessment in Fluorescence Microscopy

Hyejin Park^{1*} Jiwon Yoon^{1*} Sumin Park¹ Suree Kim² Sinae Jang¹ Eunsoo Lee¹
 Dongmin Kang^{1†} Dongbo Min^{1†}

{clrara, jwn, sm2023, jsa0801, eunssoo, dkang, dbmin}@ewha.ac.kr
 kimsuree@hanmail.net

¹Ewha Womans University, Seoul, South Korea

²Daesang, Seoul, South Korea

Abstract

Accurate focus quality assessment (FQA) in fluorescence microscopy remains challenging, as the stain-dependent optical properties of fluorescent dyes cause abrupt and heterogeneous focus shifts. However, existing datasets and models overlook this variability, treating focus quality as a stain-agnostic problem. In this work, we formulate the task of **stain-aware FQA**, emphasizing that focus behavior in fluorescence microscopy must be modeled as a function of staining characteristics. Through quantitative analysis of existing datasets (FocusPath, BBBC006) and our newly curated FluoMix, we demonstrate that focus-rank relationships vary substantially across stains, underscoring the need for stain-aware modeling in fluorescence microscopy. To support this new formulation, we propose **FluoMix**, the first dataset for stain-aware FQA that encompasses multiple tissues, fluorescent stains, and focus variations. Building on this dataset, we propose **FluoCLIP**, a two-stage vision-language framework that leverages CLIP’s alignment capability to interpret focus quality in the context of biological staining. In the **stain-grounding phase**, FluoCLIP learns general stain representations by aligning textual stain tokens with visual features, while in the **stain-guided ranking phase**, it optimizes stain-specific rank prompts for ordinal focus prediction. Together, our formulation, dataset, and framework establish the first foundation for **stain-aware FQA**, and **FluoCLIP** achieves strong generalization across diverse fluorescence microscopy conditions.

1. Introduction

Fluorescence microscopy enables high-resolution visualization of cellular and molecular structures by detecting light emitted from fluorophore-labeled targets, unlike bright-field

imaging that relies on reflected or absorbed light [8, 15, 17]. This capability makes it indispensable in biomedical research and digital pathology, where quantitative image analysis critically depends on acquiring in-focus images. However, automatic Focus Quality Assessment (FQA) in fluorescence microscopy remains largely underexplored.

Focus degradation varies fundamentally differently between the two modalities. In bright-field microscopy, blur tends to be spatially uniform, allowing low-level cues such as edges or gradients to reliably indicate focus. In contrast, fluorescence microscopy exhibits stain-dependent and non-uniform blur, since each fluorophore has distinct emission, signal-to-noise ratio, and background fluorescence. The perceived sharpness therefore varies with stain type and optical conditions, violating the underlying assumptions of conventional focus metrics. This modality gap poses critical challenges for FQA models. Thus, simple edge-based models such as FocusLiteNN [19], which performs reliably on bright-field datasets like FocusPath [11], fail to generalize to fluorescence datasets such as BBBC006 [14] and our newly curated FluoMix (Fig. 1). Their reliance on spatial gradients ignores stain-dependent variations, leading to unstable performance across fluorophores and tissue types. These observations highlight the need for stain-aware modeling capable of handling the heterogeneous focus degradation unique to fluorescence imaging.

Despite this need, existing datasets fail to capture the stain-dependent variability characteristic of fluorescence microscopy. FocusPath dataset [11], designed for bright-field imaging, assumes uniform optical conditions and lacks stain variation observed in fluorescence microscopy. BBBC006 dataset [14] contains homogeneous cell-line images acquired under tightly controlled in-vitro conditions where signal variation is minimal, offering limited biological and optical diversity. In contrast, tissue-level fluorescence microscopy involves complex three-dimensional structures, heterogeneous cell populations, and spatially varying stain distributions. These factors produce intricate

*Equal contribution.

†Corresponding Author.

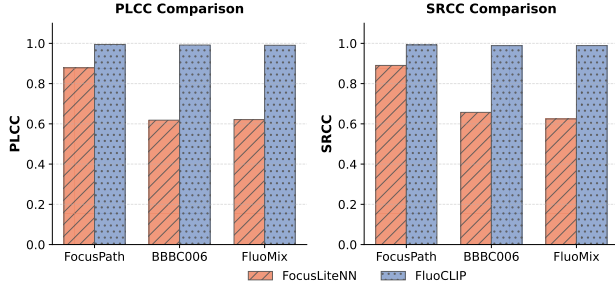


Figure 1. **Modality gap in focus quality assessment.** Simple edge-based models such as FocusLiteNN [19] perform reliably on bright-field datasets like FocusPath [11], where blur is spatially uniform, but struggles on fluorescence datasets (BBBC006 [14] and FluoMix) that exhibit stain-dependent, non-uniform defocus—underscoring the need for stain-aware FQA.

light-matter interactions and non-uniform defocus patterns that reflect real challenges in biomedical imaging.

To comprehensively capture these factors, we construct **FluoMix**, a new dataset for Stain-Aware FQA in fluorescence microscopy. FluoMix contains multi-stain, tissue-level fluorescence images acquired under varying optical conditions, providing controlled yet diverse focus variations. By reflecting the spatial and biological heterogeneity of real tissue specimens, it establishes a practical foundation for developing and evaluating models capable of robust, stain-aware focus assessment.

Building upon this dataset, we introduce **FluoCLIP**, a vision-language framework that extends CLIP-style multi-modal learning [16] to focus quality assessment in fluorescence microscopy. Unlike bright-field imaging, focus perception in fluorescence microscopy depends not only on spatial sharpness but also on the spectral and semantic properties of stains. This motivates the use of a multi-modal approach, where textual stain descriptions provide complementary cues that visual features alone cannot capture. However, pretrained CLIP encoders lack grounding in such domain-specific concepts. Textual stain descriptions (e.g., “DAPI” or “Alexa-488”) have no learned visual or semantic correspondence in the original CLIP vocabulary. As a result, the model cannot directly associate stain identity with the focus patterns characteristic of each fluorophore. Moreover, stain identity and focus quality are inherently entangled in fluorescence images, making it difficult for a single-stage alignment strategy to separate stain semantics from focus-related variations.

To address these limitations, FluoCLIP adopts a two-stage learning strategy. In the **stain-grounding phase**, the model aligns learnable stain tokens with CLIP visual features, allowing the text-side representations to acquire fluorophore-specific semantics that are absent from the pre-trained vocabulary. In the subsequent **stain-guided ranking phase**, the learned stain embeddings guide ordinal focus

prediction, enabling the model to modulate its focus perception according to stain-dependent appearance changes. This progressive design mitigates the semantic mismatch inherent in the original CLIP text encoder and disentangles stain semantics from focus-related variations.

We highlight our contributions as follows:

- We propose **FluoCLIP**, a two-stage ordinal vision-language framework that learns stain-specific grounding and stain-guided ranking for robust FQA.
- We introduce **FluoMix**, a new dataset featuring diverse fluorescent stains and tissue-level focus variations, providing the first dataset for stain-aware FQA in fluorescence microscopy.
- We formulate the task of **Stain-Aware FQA** in fluorescence microscopy, highlighting the need to model stain-dependent focus behavior.

2. Related Work

2.1. Microscopy Focus Quality Assessment

Early approaches to focus quality assessment (FQA) in microscopy adapted traditional image quality metrics such as entropy, histogram analysis, and power spectrum statistics. For example, Bray et al. [3] proposed the Power Log-Log Slope (PLLS) method, which analyzes the frequency spectrum to detect focus loss, while Koho et al. [12] utilized statistical measures to quantify sharpness. However, these hand-crafted methods are sensitive to staining variability and lack generalizability across imaging protocols.

With the rise of deep learning, data-driven methods have improved FQA robustness. Yang et al. [20] synthesized defocus using the point spread function and trained models with ordinal regression loss to reflect the ordered nature of focus levels. Albuquerque et al. [2] introduced a microscopy-specific ordinal loss, later applied to other biomedical tasks like cell development stage classification. Zhang et al. [21] further incorporated gradient maps and label distribution learning, while Gu [9] proposed training with sharp-blurred image pairs to enhance generalization.

Nonetheless, most of these models are trained on bright-field images with stable staining and gradual focus variation. In contrast, fluorescence microscopy presents abrupt focus shifts, light scattering, and stain-specific emission properties that complicate focus modeling. These challenges demand methods that can integrate both structural sharpness and stain semantics to improve focus quality estimation. This motivates exploring vision-language pretraining for microscopy focus modeling, where textual stain descriptions can complement purely visual FQA features.

2.2. CLIP for Ordinal Regression

Recent research has adapted CLIP [16] to ordinal regression by treating it as a vision-language matching problem.

Each ordinal level is encoded as a prompt, and image classification is performed by measuring similarity in the joint embedding space.

OrdinalCLIP [13] introduced rank-aware prompting, where intermediate prompts are generated via linear interpolation between base rank prompts (e.g., “age 0” and “age 100”) in the text embedding space. This preserves ordinal structure but does not explicitly ensure semantic alignment between visual and textual modalities, limiting performance in tasks with fine-grained visual differences. To address this, L2RCLIP [18] proposed RankFormer, a token-level prompt tuning module, and introduced a cross-modal pairwise ranking loss to reinforce alignment between image features and ordinal prompt ordering. This model better captures semantic ordering across modalities. NumCLIP [6] further argued that CLIP lacks numerical understanding and proposed a two-stage learning scheme that disentangles numerical semantics from natural language, improving performance in score- or quantity-based prediction tasks.

Domain-specific variants such as BiomedCLIP [22] extend CLIP pretraining to biomedical datasets and improve alignment for radiology and pathology images. However, these models are trained on text–image pairs describing anatomical or disease entities, not stain-level fluorescence characteristics, and therefore remain limited in capturing stain semantics essential for focus modeling

While prior CLIP-based ordinal models have focused on natural or radiological imagery, our work extends this paradigm to fluorescence microscopy, where ordinal cues are intertwined with stain-dependent optical effects. To this end, we introduce a two-stage training framework that first learns stain-specific visual–textual alignment and then performs stain-conditioned rank learning, enabling robust and semantically consistent focus prediction across diverse fluorescence microscopy conditions.

3. Stain-Aware Focus Quality Assessment

3.1. Problem Statement

Focus Quality Assessment (FQA) in fluorescence microscopy can be naturally formulated as an ordinal regression task, where each z -stack slice is assigned a discrete focus level from a finite, ordered set. Let $\mathcal{X} = \{x_i\}_{i=1}^N$ denote a collection of fluorescence microscopy images, and $\mathcal{Y} = \{r_i\}_{i=1}^N$ the ground truth focus ranks, where $r_i \in \{1, 2, \dots, K\}$ and K denotes the total number of focus levels. The objective is to learn a model that maps each image x_i to its ordinal rank r_i by jointly capturing structural sharpness and stain-dependent semantics that influence focus perception.

Inspired by recent CLIP-based vision-language frameworks [16], we reformulate this problem as a text-image matching task. Specifically, we use a pretrained CLIP im-

age encoder to extract visual features $v_i = E_{\text{img}}(x_i)$, and construct a set of textual templates $\mathcal{P} = \{\mathcal{P}_1, \mathcal{P}_2, \dots, \mathcal{P}_K\}$ that represent ordinal focus levels, such as “fluorescence image with focus level 1” to “fluorescence image with focus level K ”. These prompts are tokenized and encoded via the CLIP text encoder into classifier weights $t_k = E_{\text{text}}(\mathcal{P}_k)$. The cosine similarity between image x_i and rank prompt \mathcal{P}_k is computed as:

$$z_{i,k} = \langle v_i, t_k \rangle, \quad \text{for } k = 1, \dots, K \quad (1)$$

where k indexes a focus level. The predicted focus level is obtained as

$$\hat{r}_i = \arg \max_k z_{i,k}. \quad (2)$$

While this formulation enables CLIP to perform ordinal prediction via prompt-based classification, it inherently assumes that both visual and textual embeddings are semantically aligned in a domain-agnostic manner. In fluorescence microscopy, however, focus quality is governed by stain-dependent optical phenomena, including light scattering, photobleaching, and fluorophore emission variability, that generic CLIP prompts neither describe nor align with. This motivates a stain-aware adaptation that grounds textual embeddings in fluorescence-specific semantics.

3.2. FluoCLIP: Stain-Aware FQA Framework

We propose FluoCLIP, a two-stage vision-language framework for stain-aware focus quality assessment (Fig. 2). In the first stage, the model performs **stain grounding**, learning to align textual stain tokens with CLIP visual representations so that the text encoder acquires fluorescence-specific semantics. Rather than fine-tuning the CLIP text encoder, which may cause semantic drift, we keep it frozen and attach a compact adapter that learns stain-specific attributes. This design preserves the linguistic consistency of the pretrained text encoder while enabling controlled adaptation with diverse stains. In the second stage, **stain-guided ranking**, the learned stain embeddings are used to condition focus prediction on stain-dependent appearance variations. Through this process, FluoCLIP learns how focus perception varies not only with the degree of defocus but also with the emission and scattering characteristics unique to each fluorophore.

3.2.1. Stage 1: Stain-Grounding

The pretrained CLIP text encoder, trained on general web data with no exposure to fluorescence-related terminology or visual semantics, is inherently ill-suited for modeling the fluorescence-specific characteristics of stains. As shown in Table 6, directly inserting stain tokens into textual prompts without adaptation results in a noticeable drop in performance, confirming this domain gap. To address this, we introduce a stain-grounding stage that explicitly aligns textual

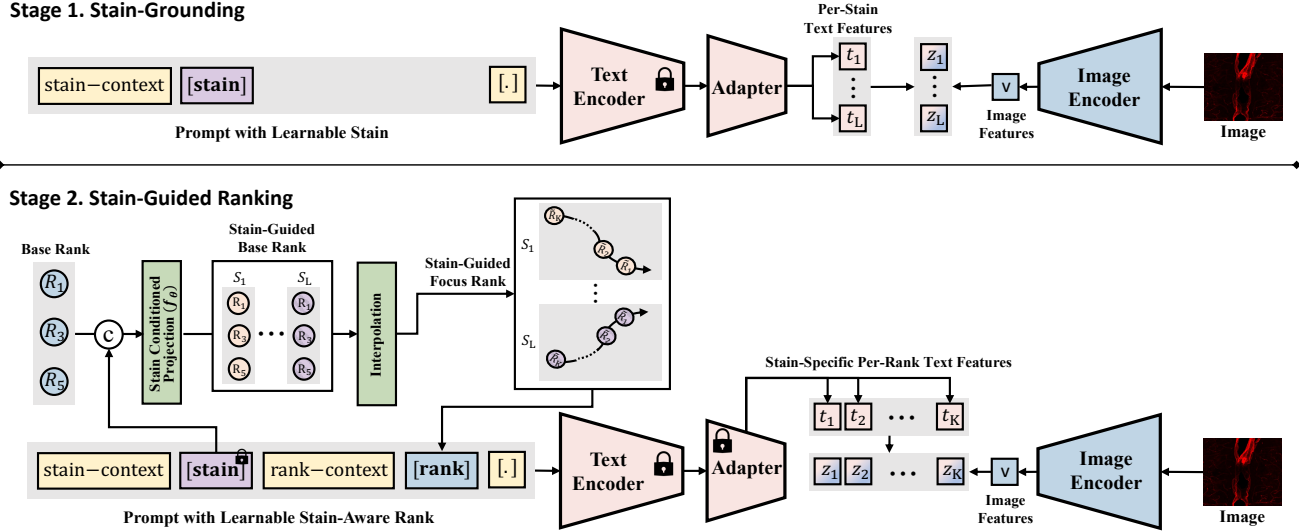


Figure 2. **Overview of FluoCLIP Framework.** FluoCLIP consists of two sequential stages for stain-aware focus quality assessment (FQA). In the *Stage 1: Stain-Grounding*, learnable stain tokens are aligned with CLIP’s visual encoder through an adapter to form stain-specific textual features. In the *Stage 2: Stain-Guided Ranking*, these grounded stain embeddings are used to condition rank prompts via interpolation and projection, producing stain-aware focus rank representations. Both stages jointly enable FluoCLIP to model stain-dependent focus behavior and align text–image features for stain-aware FQA.

stain embeddings with CLIP visual encoder. Instead of fine-tuning the pretrained text encoder, which often causes semantic drift and degrades the stability of multimodal alignment, we freeze the pretrained text encoder and instead optimize newly introduced stain embeddings and lightweight adapter layers appended to the text encoder.

Given a predefined set of L stains, each stain description is tokenized and embedded using CLIP’s token embedding layer. Let $\mathbf{S} = \{\mathbf{S}_l\}_{l=1}^L$ denote a collection of learnable stain embeddings, where each $\mathbf{S}_l \in \mathbb{R}^{C \times D}$ represents the token-level embedding sequence for stain s_l (C : the number of tokens per stain, D : embedding dimension). These embeddings are grounded to the CLIP visual encoder to encode fluorophore-specific characteristics.

To integrate stain tokens into CLIP’s textual space, we construct pseudo-sentences of the form (Fig. 2):

$$\mathcal{P}_l^{\text{stain}} = \text{Concat}([context], [\mathbf{S}_l]), \quad \text{for } l = 1, \dots, L, \quad (3)$$

where $[context]$ denotes the base prompt and $[\mathbf{S}_l]$ the learnable stain tokens. The operator $\text{Concat}(\cdot)$ represents token-level concatenation along the sequence dimension.

A lightweight adapter module, consisting of a single self-attention layer and a two-layer MLP, facilitates interaction between context and stain tokens, enabling the encoder to refine their joint representation. By optimizing only these stain-related parameters, the model learns stain-aware textual embeddings aligned with CLIP visual features, providing fluorescence-specific semantic grounding and a biologically meaningful initialization for the subsequent stain-guided ranking stage.

Given an image x_i with the ground truth stain label s_i , its visual feature is obtained as $v_i = E_{\text{img}}(x_i)$. From the text side, the stain prompts $\mathcal{P}^{\text{stain}} = \{\mathcal{P}_1^{\text{stain}}, \dots, \mathcal{P}_L^{\text{stain}}\}$ in (3) are encoded by the text encoder as $T^{\text{stain}} = E_{\text{text}}(\mathcal{P}^{\text{stain}})$. The cosine similarity between x_i and each stain prompt is then computed as

$$z_{i,l}^{\text{stain}} = \langle v_i, t_l^{\text{stain}} \rangle, \quad \text{for } l = 1, \dots, L, \quad (4)$$

where $t_l^{\text{stain}} \in T^{\text{stain}}$. The alignment is optimized in a way of predicting the stain label using the cross-entropy and KL-divergence objectives described in Sec. 3.3. This process aligns each image feature with the correct stain embedding, encouraging the model to capture fluorophore-specific semantics in the shared vision–language space.

3.2.2. Stage 2: Stain-Guided Ranking

In fluorescence microscopy, each stain exhibits a distinct relationship between focus and image appearance, producing stain-specific feature distributions that a single shared ranking space cannot capture. To handle this heterogeneity, we introduce a stain-guided embedding space that conditions the rank representation on the stain identity learned in Stage 1.

To preserve the ordinal continuity between focus levels, we follow the interpolation strategy introduced in Ordinal-CLIP [13]. A small number of base rank embeddings represent boundary ranks (*e.g.*, most- and least-focused), and intermediate ranks are obtained through weighted interpolation between them. This design encourages smooth tran-

sitions in the rank embedding space and stabilizes ordinal reasoning across focus levels.

Let $\mathbf{R}^{\text{base}} = \{\mathbf{R}_{k'}^{\text{base}}\}_{k'=1}^{K'}$ denote K' base rank embeddings, where $\mathbf{R}_{k'}^{\text{base}} \in \mathbb{R}^{C \times D}$. Given the stain embedding \mathbf{S}_l learned in Stage 1 for $l = 1, \dots, L$, a lightweight conditioning network f_θ projects each base rank embedding into a stain-guided space:

$$\mathbf{R}_{k'}^l = f_\theta(\mathbf{R}_{k'}^{\text{base}}, \mathbf{S}_l). \quad (5)$$

The resulting $\mathbf{R}_{k'}^l$ represents the stain-conditioned rank embedding. Each base rank prompt is modulated by the l^{th} stain semantics, enabling FluoCLIP to capture stain-specific focus behavior.

Finally, within each stain we generate intermediate ranks by interpolating the stain-guided base ranks:

$$\tilde{\mathbf{R}}_k^l = \sum_{k'=1}^{K'} w_{r,k'} \mathbf{R}_{k'}^l, \quad \text{for } k = 1, \dots, K, \quad (6)$$

where $w_{r,k'}$ is a predefined interpolation weight for an inverse interpolation between base ranks [13].

For an input image x_i with stain label s_i , the stain-conditioned rank embeddings are inserted into pseudo-sentence templates (Fig. 2):

$$\mathcal{P}_k^{\text{rank},i} = \text{Concat}([\textit{stain-context}], [\mathbf{S}_{s_i}], [\textit{rank-context}], [\tilde{\mathbf{R}}_k^{s_i}]), \quad (7)$$

where \mathbf{S}_{s_i} is the stain embedding corresponding to the stain s_i of image x_i , and $\tilde{\mathbf{R}}_k^{s_i}$ is the k -th interpolated rank embedding conditioned on stain s_i . The resulting prompt sequence $\mathcal{P}_k^{\text{rank},i}$ is then passed through the CLIP text encoder to obtain the final rank-aware textual representation, which is inherently sample-dependent due to its reliance on the stain s_i . A set of stain-guided rank prompts $\mathcal{P}^{\text{rank},i} = \{\mathcal{P}_1^{\text{rank},i}, \dots, \mathcal{P}_K^{\text{rank},i}\}$ is encoded as

$$t^{\text{rank},i} = \mathbf{E}_{\text{text}}(\mathcal{P}^{\text{rank},i}), \quad (8)$$

where $t^{\text{rank},i} = \{t_1^{\text{rank},i}, \dots, t_K^{\text{rank},i}\}$. The similarity between x_i and each rank prompt is defined as

$$z_k^{\text{rank},i} = \langle v_i, t_k^{\text{rank},i} \rangle, \quad \text{for } k = 1, \dots, K, \quad (9)$$

where $\langle \cdot, \cdot \rangle$ denotes cosine similarity, and $v_i = \mathbf{E}_{\text{img}}(x_i)$ is the visual embedding. These similarities are trained to predict the focus label using the cross-entropy and KL-divergence objectives described in Sec. 3.3, with the ground truth focus label $r_i \in \{1, \dots, K\}$.

3.3. Overall Training Objective

Loss Functions. FluoCLIP produces two types of similarities during training: stain-alignment similarities $z_{i,l}^{\text{stain}}$ from Stage 1 (Eq. 4) and stain-guided ranking similarities $z_{i,r}^{\text{rank}}$ from Stage 2 (Eq. 9). Following [13], both are optimized

using two complementary objectives: a cross-entropy loss \mathcal{L}_{CE} for image-to-text alignment and a KL-divergence loss \mathcal{L}_{KL} to enforce ordinal consistency in the similarity distributions. The full training objective combines the two losses:

$$\mathcal{L}_{\text{total}} = \alpha \cdot \mathcal{L}_{CE} + \beta \cdot \mathcal{L}_{KL}, \quad (10)$$

where α and β are set to 1.0 in our experiments.

4. FluoMix for Stain-Aware FQA

4.1. Motivation and Design Principles

Existing datasets for focus quality assessment (FQA) are limited in scope and fail to represent the diversity of fluorescence microscopy. FocusPath [11] is a bright-field histopathology dataset containing nine differently stained human tissues, each with 14 z-stack slices. Although it provides multiple stains, focus transitions are smooth and staining conditions are consistent across slides, making the dataset less challenging for models that rely primarily on low-level contrast cues. BBBC006 [14], on the other hand, is a fluorescence microscopy dataset of U2OS cancer cells stained with Hoechst 33342 and phalloidin. While it captures true fluorescence imaging conditions, it includes only two stains and homogeneous in-vitro cell structures, limiting its biological and optical diversity.

Consequently, existing datasets do not reflect the complexity of real-world fluorescence imaging, where multiple tissues, stains, and acquisition protocols coexist. To fill this gap, we introduce FluoMix—multi-tissue, multi-stain dataset specifically designed for stain-aware FQA in fluorescence microscopy.

4.2. FluoMix Composition

FluoMix aggregates fluorescence microscopy images across multiple tissue types and staining conditions to capture diverse optical and biological characteristics. Specifically, it includes images from **brain**, **lung**, and **liver** tissues, with up to **four distinct stains per sample**. Each field of view (FOV) is acquired as a complete **32-plane z-stack**, covering full range from sharp to severely blurred slices. In total, FluoMix contains N images spanning M unique stain-tissue combinations.

This design allows FluoMix to explicitly model *stain-dependent focus degradation*, providing a realistic dataset for testing Stain-Aware FQA methods. Alongside the raw images, we provide detailed **metadata** describing the stain identity, target protein, and acquisition protocol, enabling multimodal research, including vision–language modeling, beyond conventional image-only baselines. Representative visual examples are provided in the Supplementary Material.

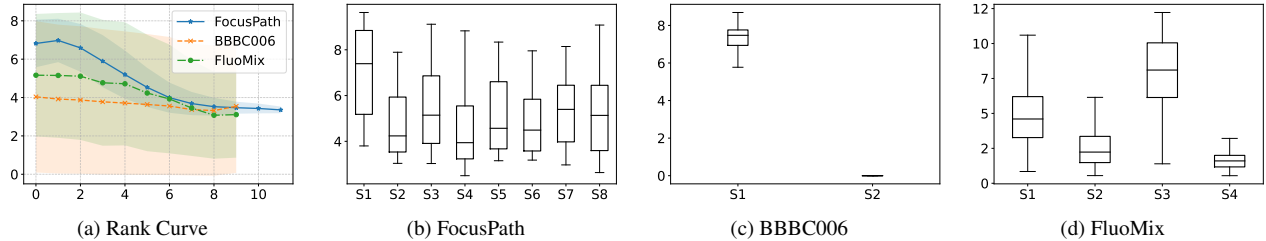


Figure 3. Empirical Analysis of Stain-Dependent Focus Behavior: (a) Mean spatial frequency (SF) versus focus rank for three datasets; the shaded region indicates ± 1 standard deviation across samples. SF decreases monotonically with increasing rank, confirming that SF reliably captures focus degradation. (b)–(d) Boxplots of SF values across stains for each dataset (x-axis: stain identity, y-axis: SF distribution). FocusPath shows stain-invariant SF trends, whereas BBBC006 and FluoMix display pronounced stain-dependent variability.

4.3. Annotation Protocol

We adopt a relative annotation scheme inspired by prior work [11]. For each z-stack, the visually best-focused slice is selected by an expert as a reference, and all other slices are assigned **relative focus levels** from 0 (best focus) to $R-1$ (worst). In this release, we provide annotations with $R = 10$ discrete ordinal levels obtained by uniformly partitioning the 32 slices.

This strategy offers a consistent yet scalable protocol for large-scale datasets, while maintaining ordinal relationships essential for FQA. Importantly, the full raw z-stacks are released so that future work can explore alternative annotation schemes—such as continuous scores, perceptual metrics, or data condensation approaches—without re-acquisition overhead. By decoupling dataset release from a fixed labeling protocol, FluoMix provides a flexible foundation for future research in *stain-aware FQA modeling*.

5. Empirical Analysis of Stain-Dependent Focus Behavior

Having introduced the dataset design, we next analyze how focus–rank relationships vary across **FocusPath** [11], **BBBC006** [14], and our proposed **FluoMix** to empirically validate the need for stain-aware focus modeling. The spatial frequency (SF) metric quantifies the density of high-frequency components in an image. Since well-focused images preserve high-frequency details while defocus attenuates them, SF serves as an effective proxy for sharpness and focus quality. We therefore use the spatial frequency (SF) metric as a quantitative measure to compare how focus behavior differs between bright-field and fluorescence modalities. Further explanation about SF metric are provided in the Supplementary Material.

5.1. Per-Rank Behavior of Sharpness Metric

We first examine the relationship between the spatial frequency (SF) metric and the discrete focus ranks to verify that the metric reliably reflects the degree of defocus represented by the ranks. As shown in Fig. 3(a), the mean SF values exhibit a generally monotonic decrease as the focus

level moves from in-focus to defocused regions across all three datasets. This confirms that the SF metric can reasonably capture the overall directionality of focus degradation implied by the ordinal labels, validating its use as a quantitative sharpness indicator for subsequent analysis. In other words, while focus ranks are discrete and manually defined, the SF metric provides as an objective, continuous indicator of focus quality, exhibiting a strong correlation with the discrete rank progression.

5.2. Stain-Wise Variability Across Datasets

We then analyze the distribution of the SF metric across different stains within each dataset in Fig. 3. In FocusPath [11], which consists of bright-field H&E-stained whole-slide images, the per-stain variance is modest, with stains exhibiting closely aligned SF ranges and largely overlapping distributions, indicating stain-invariant focus behavior. In contrast, BBBC006 [14] and FluoMix exhibit substantial stain-dependent variability. Different fluorescent stains occupy distinct SF ranges with largely non-overlapping variances, demonstrating that focus degradation is highly stain-dependent in fluorescence microscopy. This observation supports the hypothesis that focus quality should be modeled as a function of stain characteristics rather than assuming a universal focus–rank mapping.

5.3. Sharpness Metric and Rank Correlation

To further quantify this effect, we compute the Spearman rank correlation coefficient (SRCC) between focus rank and SF metric for each stain. Since spatial frequency decreases as defocus increases, SF monotonically decreases with rank. This produces an inherently negative SRCC value, where the absolute magnitude $|\rho|$ reflects the strength of the relationship: larger values indicate that SF aligns more consistently with the underlying focus levels. As shown in Table. 1, FocusPath [11] achieves the highest correlation, indicating that its ordinal labels correspond closely to actual blur magnitudes under stain-invariant conditions. However, correlations drop significantly in BBBC006 [14] and FluoMix, revealing that rank–blur consistency weakens in fluorescence microscopy due to heterogeneous optical

Table 1. Spearman Rank Correlation Coefficient (SRCC) statistics of the Spatial Frequency (SF) metric and focus rank. The results reported are mean \pm standard deviation across all stains in each datasets.

Metric	FluoMix	FocusPath	BBBC006
SRCC ρ	-0.528 \pm 0.0940	-0.840 \pm 0.0923	-0.343 \pm 0.2920

Table 2. Comparison of FluoCLIP with existing methods using a ResNet50 image encoder on FluoMix. The results are mean \pm standard deviation over five runs with different random seeds.

Method	Accuracy (%)	PLCC \uparrow	SRCC \uparrow	MAE \downarrow
FocusLiteNN	-	0.621 \pm 0.0042	0.624 \pm 0.0047	1.610 \pm 0.0058
CE	54.59 \pm 1.42	0.952 \pm 0.0023	0.957 \pm 0.0017	0.510 \pm 0.0148
OE	63.46 \pm 1.38	0.966 \pm 0.0019	0.969 \pm 0.0017	0.395 \pm 0.0171
CO2	47.26 \pm 1.99	0.927 \pm 0.0054	0.931 \pm 0.0052	0.653 \pm 0.0335
QULCE	55.55 \pm 2.12	0.951 \pm 0.0050	0.957 \pm 0.0041	0.512 \pm 0.0320
OrdinalCLIP	83.12 \pm 0.41	0.989 \pm 0.0006	0.988 \pm 0.0005	0.172 \pm 0.0049
NumCLIP	-	0.985 \pm 0.0004	0.985 \pm 0.0005	0.325 \pm 0.0054
FluoCLIP	85.21\pm0.88	0.991\pm0.0006	0.989\pm0.0004	0.150\pm0.0087

Table 3. Performance comparison of CLIP-based models with existing methods using a ViT/B-16 image encoder on FluoMix. The results are mean \pm standard deviation over five runs with different random seeds.

Method	Accuracy (%)	PLCC \uparrow	SRCC \uparrow	MAE \downarrow
OrdinalCLIP	89.95 \pm 0.31	0.993 \pm 0.0002	0.991 \pm 0.0002	0.102 \pm 0.0032
NumCLIP	-	0.987 \pm 0.0014	0.988 \pm 0.0003	0.133 \pm 0.0031
BiomedCLIP	83.99 \pm 0.25	0.990 \pm 0.0003	0.988 \pm 0.0003	0.163 \pm 0.0027
FluoCLIP	90.75\pm0.52	0.994\pm0.0005	0.992\pm0.0004	0.093\pm0.0055

properties across stains. This reduced correlation implies that a single, stain-agnostic ranking model cannot reliably capture focus variation across fluorescence conditions.

Summary. These analyses demonstrate that while bright-field microscopy exhibits uniform, stain-independent focus behavior, fluorescence microscopy shows strong stain-specific trends and inconsistent rank-focus correlations. Therefore, accurate focus quality assessment in fluorescence microscopy requires a **stain-aware ordinal framework** capable of modeling these stain-conditioned focus variations.

6. Experiments

6.1. Datasets and Experiment Settings

Datasets. All experiments were conducted with consistent training protocols across FocusPath [11], BBBC006 [14], and FluoMix. Within FluoMix, brain tissue images were used for training, and images from other tissues were used for validation and few-shot testing to assess cross-tissue generalization.

Training Details. We adopted CLIP [16] as the vision-language backbone. Image encoder was initialized from either CLIP-pretrained ResNet50 [10] or ViT-B/16 [5] backbone, with its pretrained counterparts and random initial-

Table 4. Comparison of FluoCLIP with existing methods using a ResNet50 image encoder on BBBC006 [14]. The results are mean \pm standard deviation over five runs with different random seeds.

Method	Accuracy (%)	PLCC \uparrow	SRCC \uparrow	MAE \downarrow
FocusLiteNN	-	0.618 \pm 0.0062	0.657 \pm 0.0080	1.599 \pm 0.6571
CE	75.71 \pm 8.24	0.973 \pm 0.0102	0.975 \pm 0.0091	0.266 \pm 0.0928
OE	75.03 \pm 12.55	0.967 \pm 0.0176	0.969 \pm 0.0159	0.296 \pm 0.1565
CO2	68.84 \pm 3.91	0.965 \pm 0.0056	0.968 \pm 0.0050	0.347 \pm 0.0469
QULCE	75.25 \pm 7.57	0.962 \pm 0.0123	0.965 \pm 0.0109	0.301 \pm 0.1069
OrdinalCLIP	90.67 \pm 0.54	0.991 \pm 0.0004	0.989\pm0.0002	0.104 \pm 0.0058
NumCLIP	-	0.973 \pm 0.0009	0.980 \pm 0.0006	0.249 \pm 0.0051
FluoCLIP	93.05\pm0.34	0.992\pm0.0005	0.989\pm0.0004	0.080\pm0.0046

Table 5. Comparison of FluoCLIP with existing methods using a ResNet50 image encoder on FocusPath [11]. The results are mean \pm standard deviation over five runs with different random seeds.

Method	Accuracy (%)	PLCC \uparrow	SRCC \uparrow	MAE \downarrow
OrdinalCLIP	94.98 \pm 0.99	0.997 \pm 0.0006	0.993 \pm 0.0004	0.051 \pm 0.0099
FluoCLIP	91.11 \pm 1.40	0.995 \pm 0.0007	0.992 \pm 0.0005	0.092 \pm 0.0142

ized prompts. Each baseline model was trained using the RAdam optimizer and a cosine learning rate scheduler. For FluoCLIP, we adopted a two-stage training protocol consisting of 10 epochs for the *Stain-Grounding* stage and 100 epochs for the *Stain-Guided Ranking* stage. All other training settings, including data preprocessing and augmentations, were kept identical across models. Input images were resized to 256×256 , randomly cropped to 224×224 , and augmented using horizontal flips and standard normalization.

Baselines. We compared our FluoCLIP against FocusLiteNN [19], OrdinalCLIP [13], NumCLIP [6], BiomedCLIP [22] and standard baselines including Cross-Entropy (CE), Ordinal Encoding (OE) [4], CO2 [1], and QULCE [2]. For fair comparison, all baselines were experimented using the same ResNet50 encoder and respective loss functions. FocusLiteNN was evaluated separately using its original lightweight CNN architecture due to structural incompatibility with our framework.

Evaluation Metrics. Performance was evaluated using classification accuracy, PLCC (Pearson linear correlation), SRCC (Spearman rank correlation), and MAE (mean absolute error). To compute PLCC, SRCC, and MAE, the predicted focus level is given by $\hat{y} = \sum_{j=0}^{M-1} p_j \cdot j$, where p_j is the probability of focus level j , and M is the total number of discrete ranks.

6.2. Comparative Study

Results on FluoMix. FluoMix presents the greatest challenge due to its high stain variability and heterogeneous tissue structures. Traditional models exhibit significant drops in performance, with accuracy ranging from 47.26 \pm 1.99% to 63.46 \pm 1.38%, indicating their inability to adapt to diverse staining conditions. In contrast, FluoCLIP achieves

Table 6. Ablation study on FluoCLIP components on the FluoMix dataset. The baseline (OrdinalCLIP [13]) includes only the focus token. We incrementally add grounded stain tokens (C) and stain-guided rank modules (D) to evaluate their individual contributions.

Type	Configuration	R	S^{plain}	S^{train}	S	\bar{R}^S	Acc. (%)	Step Gain	Total Gain
(A)	Baseline (OrdinalCLIP) with Rank (R)	✓					83.12	-	-
(B)	(A) + Plain Stain Token (S^{plain})	✓	✓				82.47	-0.64	-
(C)	(A) + Learnable Stain Token (S^{train})	✓		✓			80.05	-2.62	-
(D)	(A) + Grounded Stain Token (S)				✓	✓	84.28	1.16	1.16
(E)	(D) + Stain-Guided Rank Token (\bar{R}^S)				✓	✓	85.21	0.93	2.09

85.21±0.88% (Table 2), substantially outperforming all baselines. The explicit integration of stain-specific text tokens with stain-conditioned rank prompts allows FluoCLIP to model complex stain-dependent focus variations that conventional FQA models cannot capture. FluoCLIP also maintains its advantage with a ViT-B/16 encoder (Table 3), demonstrating strong robustness across architectures.

Results on BBBC006. BBBC006 [14] contains fluorescence images of U2OS cells with limited stain diversity and clear cell structures. Conventional FQA models and lightweight CNNs such as FocusLiteNN [19] fail to capture subtle focus variations. FluoCLIP achieves 93.05% accuracy (Table 4), surpassing OrdinalCLIP by 2.4% while maintaining lower variance. These results indicate that even in relatively homogeneous fluorescence datasets, explicit stain conditioning improves focus estimation by increasing sensitivity to stain-specific optical cues.

Results on FocusPath. FocusPath [11] consists of bright-field H&E slides where focus variations are relatively uniform and stain-invariant across focal planes. Under these homogeneous conditions, conventional FQA models already achieve near-optimal performance. Adding stain-conditioned prompts in FluoCLIP introduces unnecessary modeling capacity and slightly disrupts this smooth rank structure, resulting in a modest drop in accuracy (Table 5). This behavior aligns with our design hypothesis that stain-aware modeling is most beneficial in fluorescence settings with strong stain-dependent variability, but offers limited or negative gains in stain-invariant bright-field datasets.

6.3. Ablation Study

Contribution of Individual Components. Explicit stain alignment and stain-conditioned ranking are critical to FluoCLIP. We validate this on FluoMix using a ResNet-50 CLIP backbone. Table 6 summarizes the results. The baseline (A), identical to OrdinalCLIP [13], achieves 83.12% accuracy. Adding a non-learnable stain token (B) slightly decreases accuracy by 0.64%, indicating that simply appending stain information is ineffective because CLIP has no prior knowledge of fluorescence-specific stain semantics. Even when the stain token is made learnable (C), accuracy drops more substantially (-2.62%), showing that introducing trainable text parameter without explicitly aligning them to visual features can inject uninformative or noisy semantics that interfere with learning. Introducing learn-

Table 7. Performance Evaluation of FluoCLIP using BiomedCLIP [22] and OrdinalCLIP [13] as backbones. (A)–(C) use BiomedCLIP, while (D) corresponds to our main model based on CLIP ViT-B-16. Results are reported as mean ± standard deviation over five runs on FluoMix.

Type	Configuration	Accuracy (%)	PLCC ↑	SRCC ↑	MAE ↓
(A)	BiomedCLIP	83.99±0.25	0.990±0.0003	0.988±0.0003	0.163±0.0027
(B)	(A) + S^{plain}	84.35±0.27	0.990±0.0002	0.9883±0.0002	0.159±0.0027
(C)	(B) + \bar{R}^S	86.29±0.51	0.991±0.0004	0.989±0.0003	0.140±0.0055
(D)	FluoCLIP	90.75±0.52	0.994±0.0005	0.992±0.0004	0.093±0.0055

able stain tokens through the stain-grounding stage (D) improves accuracy to 84.28%, confirming the benefit of learning stain-visual correlations. Finally, incorporating the stain-guided ranking stage (E) raises accuracy to 85.21%, a total gain of +2.09% over the baseline. These results verify that both stages contribute synergistically—progressively enhancing the model’s ability to capture stain semantics and model stain-specific focus variations.

Effects of Learning Stain Representations. The ablations on **BiomedCLIP** [22] confirm the same trend observed in Table 6—explicitly understanding stains and modeling stain-guided ranks significantly improve performance (Table 7). Despite these gains, **FluoCLIP** with the standard CLIP ViT-B/16 backbone achieves a much higher accuracy of **90.75%**, surpassing all BiomedCLIP variants. We attribute this gap to two limitations of BiomedCLIP: (1) text encoder (PubMedBERT), which lacks exposure to optical descriptors such as “sharp”, “blur” or actual non-optimal images, and (2) image encoder, which was trained on mixed biomedical imagery rather than fluorescence microscopy. These findings highlight the importance of explicitly learning stain-grounded textual embeddings, rather than relying on domain-specific pretraining alone.

7. Conclusion

We introduced the task of **stain-aware ordinal focus quality assessment (FQA)** for fluorescence microscopy, highlighting the importance of modeling stain-dependent focus behavior. To address this challenge, we proposed **FluoCLIP**, a two-stage vision–language framework that explicitly learns the interaction between fluorophore characteristics and focus quality. In the *stain-grounding* stage, learnable stain tokens are aligned with CLIP’s visual encoder, while the *stain-guided ranking* stage leverages these

aligned embeddings for stain-conditioned ordinal reasoning. Together with our dataset **FluoMix**, which covers multi-stain, tissue-level fluorescence images, FluoCLIP establishes a new foundation for robust focus assessment under biologically diverse conditions. Extensive experiments on BBBC006 and FluoMix confirm that the two-stage learning scheme progressively enhances the model’s understanding of stain semantics and consistently outperforms conventional FQA methods and recent vision–language baselines.

While FluoCLIP demonstrates strong performance, it still relies on predefined stain categories during alignment, limiting adaptation to entirely unseen stains or imaging modalities. Future work will explore automatic stain discovery and cross-channel reasoning to further generalize stain-aware FQA across broader fluorescence domains.

References

- [1] Tomé Albuquerque, Ricardo Cruz, and Jaime S Cardoso. Ordinal losses for classification of cervical cancer risk. *PeerJ Computer Science*, 7:e457, 2021. 7
- [2] Tomé Albuquerque, Ricardo Cruz, and Jaime S Cardoso. Quasi-unimodal distributions for ordinal classification. *Mathematics*, 10(6):980, 2022. 2, 7
- [3] Mark-Anthony Bray, Adam N Fraser, Thomas P Hasaka, and Anne E Carpenter. Workflow and metrics for image quality control in large-scale high-content screens. *Journal of biomolecular screening*, 17(2):266–274, 2012. 2
- [4] Jianlin Cheng, Zheng Wang, and Gianluca Pollastri. A neural network approach to ordinal regression. In *2008 IEEE international joint conference on neural networks (IEEE world congress on computational intelligence)*, pages 1279–1284. IEEE, 2008. 7
- [5] Alexey Dosovitskiy, Lucas Beyer, Alexander Kolesnikov, Dirk Weissenborn, Xiaohua Zhai, Thomas Unterthiner, Mostafa Dehghani, Matthias Minderer, Georg Heigold, Sylvain Gelly, et al. An image is worth 16x16 words: Transformers for image recognition at scale. *arXiv preprint arXiv:2010.11929*, 2020. 7
- [6] Yao Du, Qiang Zhai, Weihang Dai, and Xiaomeng Li. Teach clip to develop a number sense for ordinal regression. In *European Conference on Computer Vision*, pages 1–17. Springer, 2024. 3, 7
- [7] Ahmet M. Eskicioglu and Paul S. Fisher. Image quality measures and their performance. *IEEE Trans. Commun.*, 43: 2959–2965, 1995. 1
- [8] M Elena Garcia-Pardo, Jeremy C Simpson, and Niamh C O’Sullivan. A novel automated image analysis pipeline for quantifying morphological changes to the endoplasmic reticulum in cultured human cells. *BMC bioinformatics*, 22:1–17, 2021. 1
- [9] Yun Gu. Single-shot focus estimation for microscopy imaging with kernel distillation. *IEEE Transactions on Computational Imaging*, 2023. 2
- [10] Kaiming He, Xiangyu Zhang, Shaoqing Ren, and Jian Sun. Deep residual learning for image recognition. In *Proceedings of the IEEE conference on computer vision and pattern recognition*, pages 770–778, 2016. 7
- [11] Mahdi S Hosseini, Yueyang Zhang, and Konstantinos N Plataniotis. Encoding visual sensitivity by maxpool convolution filters for image sharpness assessment. *IEEE Transactions on Image Processing*, 28(9):4510–4525, 2019. 1, 2, 5, 6, 7, 8
- [12] Sami Koho, Elnaz Fazeli, John E Eriksson, and Pekka E Hänninen. Image quality ranking method for microscopy. *Scientific reports*, 6(1):28962, 2016. 2
- [13] Wanhua Li, Xiaoke Huang, Zheng Zhu, Yansong Tang, Xiu Li, Jie Zhou, and Jiwen Lu. Ordinalclip: Learning rank prompts for language-guided ordinal regression. *Advances in Neural Information Processing Systems*, 35:35313–35325, 2022. 3, 4, 5, 7, 8
- [14] Vebjorn Ljosa, Katherine L Sokolnicki, and Anne E Carpenter. Annotated high-throughput microscopy image sets for validation. *Nature methods*, 9(7):637–637, 2012. 1, 2, 5, 6, 7, 8
- [15] Christopher A Mela and Yang Liu. Application of convolutional neural networks towards nuclei segmentation in localization-based super-resolution fluorescence microscopy images. *BMC bioinformatics*, 22:1–30, 2021. 1
- [16] Alec Radford, Jong Wook Kim, Chris Hallacy, Aditya Ramesh, Gabriel Goh, Sandhini Agarwal, Girish Sastry, Amanda Askell, Pamela Mishkin, Jack Clark, et al. Learning transferable visual models from natural language supervision. In *International conference on machine learning*, pages 8748–8763. PMLR, 2021. 2, 3, 7
- [17] Merlin Veronika, Roy Welsch, Alvin Ng, Paul Matsudaira, and Jagath C Rajapakse. Correlation of cell membrane dynamics and cell motility. In *BMC bioinformatics*, pages 1–11. Springer, 2011. 1
- [18] Rui Wang, Peipei Li, Huaibo Huang, Chunshui Cao, Ran He, and Zhaofeng He. Learning-to-rank meets language: Boosting language-driven ordering alignment for ordinal classification. *Advances in Neural Information Processing Systems*, 36, 2023. 3
- [19] Zhongling Wang, Mahdi Hosseini, Adyn Miles, Konstantinos Plataniotis, and Zhou Wang. Focuslitenn: High efficiency focus quality assessment for digital pathology. In *Medical Image Computing and Computer Assisted Intervention – MICCAI 2020*. Springer International Publishing, 2020. 1, 2, 7, 8
- [20] Samuel J Yang, Marc Berndl, D Michael Ando, Mariya Barch, Arunachalam Narayanaswamy, Eric Christiansen, Stephan Hoyer, Chris Roat, Jane Hung, Curtis T Rueden, et al. Assessing microscope image focus quality with deep learning. *BMC bioinformatics*, 19:1–9, 2018. 2
- [21] Chuyan Zhang, Yun Gu, Jie Yang, and Guang-Zhong Yang. Diversity-aware label distribution learning for microscopy auto focusing. *IEEE Robotics and Automation Letters*, 6(2): 1942–1949, 2021. 2
- [22] Sheng Zhang, Yanbo Xu, Naoto Usuyama, Hanwen Xu, Jaspreet Bagga, Robert Tinn, Sam Preston, Rajesh Rao, Mu Wei, Naveen Valluri, Cliff Wong, Andrea Tupini, Yu Wang, Matt Mazzola, Swadheen Shukla, Lars Liden, Jianfeng Gao,

Angela Crabtree, Brian Piening, Carlo Bifulco, Matthew P. Lungren, Tristan Naumann, Sheng Wang, and Hoifung Poon. A multimodal biomedical foundation model trained from fifteen million image–text pairs. *NEJM AI*, 2(1), 2024. [3](#), [7](#), [8](#)

- [23] Kaiyang Zhou, Jinkang Yang, Chen Change Loy, and Ziwei Liu. Learning to prompt for vision-language models. *International Journal of Computer Vision*, 130(9):2337–2348, 2022. [3](#), [4](#)

FluoCLIP: Stain-Aware Focus Quality Assessment in Fluorescence Microscopy

Supplementary Material

8. Spatial Frequency

In Sec. 5, we used the spatial frequency (SF) [7] metric as a quantitative proxy for image sharpness to analyze stain-dependent focus behavior across datasets. For completeness, we provide the exact formulation of SF below.

Given an image $I \in \mathbb{R}^{M \times N}$, the row and column frequency components are defined as

$$\begin{aligned} RF &= \sqrt{\frac{1}{(M-1)N} \sum_{i=1}^{M-1} \sum_{j=1}^N (I(i+1, j) - I(i, j))^2}, \\ CF &= \sqrt{\frac{1}{M(N-1)} \sum_{i=1}^M \sum_{j=1}^{N-1} (I(i, j+1) - I(i, j))^2}, \\ SF &= \sqrt{RF^2 + CF^2}. \end{aligned} \tag{11}$$

Higher SF values indicate sharper, more in-focus images, while lower values correspond to defocus.

9. Dataset Details

9.1. Overview of Datasets

We evaluated FluoCLIP on three datasets used in Sec. 5 and Sec. 6: **FocusPath** [11], **BBBC006** [14], and our fluorescence microscopy dataset **FluoMix**. To ensure consistent training across datasets, all z-stacks were reorganized into discrete focus levels, ranging from in-focus to severely defocused, following the ordinal labeling protocol described in the main paper (Sec. 4). Representative examples from each dataset are shown in Fig. 4 and Fig. 5. The former illustrates focus-level (rank) variations across datasets, whereas the latter highlights stain-dependent visual differences across the three datasets.

9.2. BBBC006

BBBC006 dataset consists of fluorescence images of Hoechst 33342- and phalloidin-stained U2OS cells. Each field of view contains a 32-plane z-stack ($2\mu\text{m}$ spacing), with the in-focus slice at position 16. Following prior work, we relabeled the stack into 10 ordinal focus levels (0–9). In our experiments, we use 23,341 images for training and 5,843 images for testing.

9.3. FocusPath

FocusPath provides 8,640 bright-field image patches (1024×1024) from nine differently stained slides. Each patch is assigned an absolute z-level from 0 to 13. Due to

limited samples in the most defocused slices (levels 12–13), we merge them into level 11, resulting in 12 ordinal levels (0–11). We follow the standard split of 3,876 training and 972 testing samples.

9.4. FluoMix

FluoMix is a fluorescence microscopy dataset designed to capture stain-dependent variability across multiple tissues. The dataset spans three tissue types (**brain, lung, liver**) and four fluorescent channels (Hoechst 33342/34580 or DAPI, Alexa Fluor 488, Cy3, Alexa Fluor 647). Each stain channel corresponds to distinct biological targets, such as neuronal markers (NeuN, NFM, TH), microglial markers (Iba-1), vascular markers (CD31, Collagen IV), and epithelial markers (CK19, Claudin, ZO-1). Table 8 summarizes the stain-target combinations included in FluoMix.

Each field of view is acquired as a full z-stack (34 planes for FluoMix) covering the progression from in-focus to severely defocused slices. For consistency with FocusPath and BBBC006, all z-stacks are converted into **10 ordinal focus levels** (0 = in-focus, 9 = out-of-focus) using the relative labeling scheme described in Sec. 4. Representative examples are shown in Fig. 4.

For the main experiments, we used brain-tissue subset of FluoMix (D1–D4), consisting of 25,967 training and 6,506 testing images across four stain combinations.

10. FluoMix Dataset: Biological Preparation and Imaging Protocols

FluoMix was constructed from adult **rat brain, lung, and liver** tissues, following institutional ethical guidelines approved by the Institutional Review Board (IRB). All samples were processed using standardized fixation, immunostaining, and confocal imaging protocols to ensure cross-tissue consistency while preserving stain-dependent optical characteristics.

10.1. Tissue Preparation

C57BL/6J male rats (8 weeks old) were euthanized using CO_2 anesthesia (30–70% volume/min). Transcardial perfusion was performed with saline followed by fixation with 4% paraformaldehyde (PFA). Brain, lung, and liver tissues were post-fixed for 24 hours, cryoprotected in 30% sucrose, and sectioned into $40\mu\text{m}$ slices.

10.2. Immunostaining

Free-floating sections from all tissues were blocked in PBS containing 3% bovine serum albumin (BSA) and 0.1% Tri-

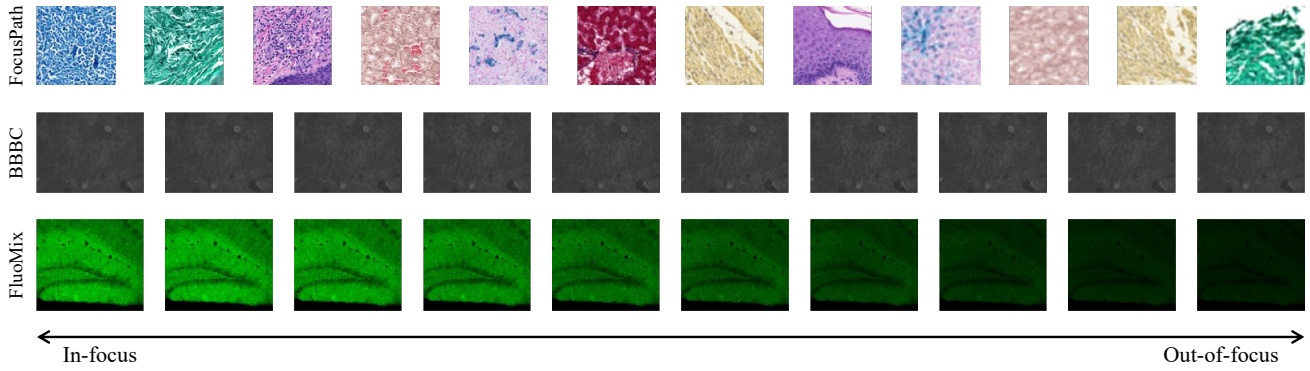


Figure 4. Examples of dataset classes: The figure displays samples of images from three datasets across different focus levels. (Top) FocusPath dataset images numbered from 0 to 11, each showing different staining techniques. (Middle) BBBC006 dataset images numbered from 0 to 9. (Bottom) FluoMix dataset images numbered from 0 to 9, representing different focus levels.

Table 8. Overview of the FluoMix dataset, summarizing tissue types, fluorescent stains, and associated biological targets. Each stain is paired with distinct protein markers (e.g., neuronal, microglial, vascular, epithelial), reflecting the heterogeneity of fluorescence signals across tissues. The rightmost column reports the number of fields of view collected for each stain–target combination.

Brain Tissue					
Dataset	Hoechst 34580	Alexa 488	Cy3	Alexa 647	# Sets
D1	nucleus	Iba-1	Tuj-1	Collagen IV	504
D2	nucleus	Neurofilament-M (NFM)	Tyrosine Hydroxylase (TH)	Collagen IV	152
D3	nucleus	NeuN	Tyrosine Hydroxylase (TH)	Collagen IV	554
D4	nucleus	GFAP	Tuj-1	CD31	623
Lung Tissue					
Dataset	Hoechst 33342	Alexa 488	Cy3	Alexa 647	# Sets
D5	nucleus	CD31	Vimentin	Collagen IV	634
D6	nucleus	CD31	Vimentin	Collagen IV	596
Liver Tissue					
Dataset	DAPI	Alexa 488	Cy3	Alexa 647	# Sets
D7	nucleus	CK19	Claudin	ZO-1	96

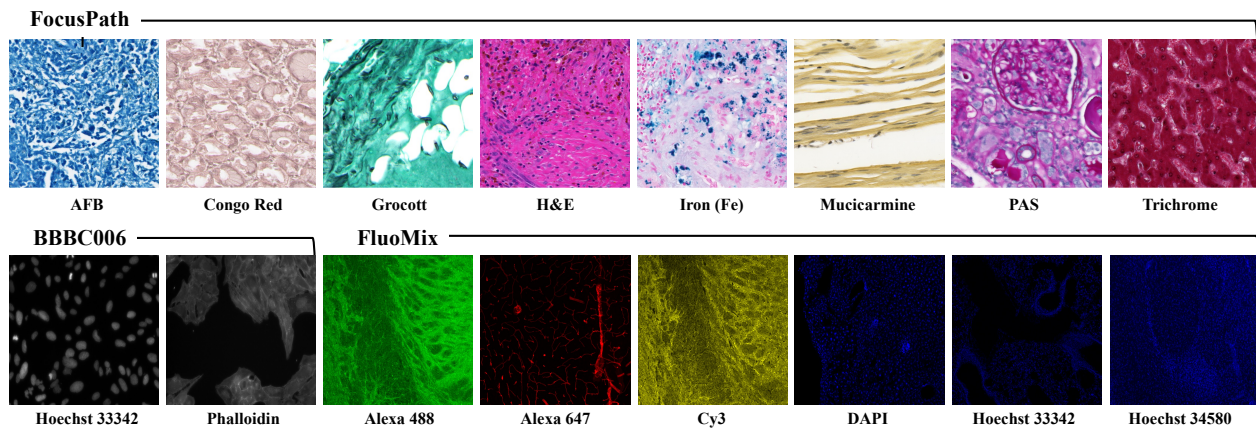


Figure 5. Sample images illustrating stain diversity in the three datasets. (Top) **FocusPath**: bright-field microscopy images with eight different histological dyes. (Bottom left) **BBBC006**: fluorescence microscopy images of cell lines labeled with Hoechst 33342 and Phalloidin. (Bottom right) **FluoMix**: tissue-level fluorescence microscopy images covering six distinct fluorescent staining protocols.

ton X-100 for 1 hour at room temperature. Slices were incubated overnight at 4°C with primary antibodies targeting diverse cellular structures, including:

- **Brain:** Iba-1, NeuN, NFM, Tuj-1, GFAP, TH, CD31, Collagen IV
- **Lung:** CD31, Vimentin, Collagen IV
- **Liver:** CK19, Claudin, ZO-1

After washing, sections were incubated with Alexa Fluor-conjugated secondary antibodies (Alexa Fluor 488, Cy3, Alexa Fluor 647). Hoechst 33342, Hoechst 34580 or DAPI (1:2000) was used to counterstain nuclei. Slides were washed, mounted with anti-fade medium, and allowed to dry under light-protected conditions.

10.3. Imaging Conditions

All fluorescence images were acquired using a Leica MICA confocal microscope with a 10× objective (NA 0.32) at a resolution of 1600 × 1352 pixels (0.586 μm/pixel). Excitation wavelengths were selected based on fluorophore spectra: 405 nm (Hoechst, DAPI), 488 nm (Alexa Fluor 488), 561 nm (Cy3), and 647 nm (Alexa Fluor 647), with matched bandpass emission filters to minimize spectral bleed-through.

To capture focus variability across staining conditions, each field of view (FOV) was acquired as a full z-stack:

- **Brain:** 34-plane stacks (1-2 μm spacing)
- **Lung:** 34-plane stacks (2 μm spacing)
- **Liver:** 34-plane stacks (2 μm spacing)

Laser power and exposure settings were adjusted per channel to optimize signal-to-noise ratio while maintaining consistency across tissue types. No deconvolution or contrast enhancement was applied to preserve the native optical properties of each stain.

11. Few-Shot Validations

Fluorescence microscopy exhibits substantial stain- and tissue-dependent variability, making it unrealistic to obtain dense focus annotations across all stain-tissue combinations encountered in practice. As a result, few-shot adaptation is a key requirement for stain-aware FQA models deployed in real imaging workflows, where supervision is scarce and domain shifts naturally arise across laboratories.

To evaluate FluoCLIP under these realistic constraints, we consider three complementary few-shot settings: (1) label-efficient learning with limited training samples, (2) generalization to unseen tissues under known stains, and (3) generalization to unseen stain-tissue pairs. As summarized in Table 9, these settings vary in whether the stain, the tissue, or both differ from the base training domain, thereby separating the effect of supervision scarcity from the effects of stain- and tissue-driven domain shifts. This structured evaluation allows us to systematically assess how well Flu-

oCLIP transfers its stain-grounded representations under increasingly challenging and practically relevant scenarios.

11.1. Few-Shot Learning on FluoMix

To evaluate whether FluoCLIP can model Stain-Aware FQA with only a small number of labeled training samples, we first perform few-shot fine-tuning on the FluoMix brain-tissue subset (D1-D4). This restricted setup allows us to assess how effectively the model learns stain-dependent focus behavior when supervision is severely limited. All methods were initialized from the same pretrained CLIP image encoder (ResNet50) and text encoders. For baselines, we finetuned CoOp [23] following the protocol from the original paper, where the encoders are frozen and only the prompt embeddings are learned. Because both OrdinalCLIP [13] and FluoCLIP update both the image encoder and text prompts, we additionally include CoOp+ E_{img} , which extends CoOp by also fine-tuning the image encoder to ensure a fair architectural comparison.

For each method, we sample k labeled samples per focus rank per stain ($k = \{1, 8, 16, 32, 64, 128\}$). Since D1-D4 contain four stain combinations and 10 ordinal focus ranks, each few-shot training set consists of $4 \times 10 \times k$ training images. Although all models start from the generic CLIP checkpoint, this experiment evaluates whether they can adapt to the fluorescence FQA domain using only this small subset. In particular, it measures how effectively each method acquires stain-aware focus behavior when fine-tuning from a natural-image pretraining domain to the fluorescence microscopy domain with extremely limited supervision. This setting allows us to directly test whether FluoCLIP’s stain-aware design provides a stronger and more data-efficient adaptation capability than stain-agnostic baselines.

Adapting from CLIP to the fluorescence FQA domain with only a handful of labeled examples is inherently challenging, particularly because stain-dependent appearance variations amplify the effect of limited supervision. Nevertheless, the few-shot results in Table 10 reveal consistent behavioral patterns across methods. **CoOp** performs the worst, and **CoOp+ E_{img}** often degrades further, consistent with observations from [23] that naive image-encoder fine-tuning can be harmful. **OrdinalCLIP** slightly outperforms FluoCLIP at very low shot counts (1–32), but its gains saturate quickly. In contrast, **FluoCLIP** exhibits the steepest improvement and ultimately achieves the best performance in the 64–128 shot range. Taken together, these results demonstrate that FluoCLIP’s stain-aware design provides a more data-efficient adaptation mechanism, enabling the model to acquire stain-dependent focus behavior more rapidly than stain-agnostic baselines once modest supervision is available.

Table 9. Overview of the three few-shot evaluation settings used to assess label efficiency, cross-stain transfer, and cross-tissue generalization.

Generalization Type	Model Initialization	Adaptation Stain	Adaptation Tissue	Description
Few-Shot Learning	CLIP-pretrained on Natural Images	Alexa 488, Cy3, Alexa 647, Hoechst 34580	Brain	Test whether the model can learn stain-aware FQA with only k-shot samples
Cross-Tissue	FluoCLIP-pretrained on Brain (D1-D4)	Alexa 488, Cy3, Alexa 647 (Seen Stains)	Lung (Unseen Tissue)	Adaptation to new tissue with distinct morphology while keeping stains unchanged
Cross-Stain & Cross-Tissue	FluoCLIP-pretrained on Brain (D1-D4)	Hoechst 33342, DAPI (Unseen Stains)	Lung, Liver (Unseen Tissues)	Most challenging: test adaptation to entirely new stain-tissue pairs

Table 10. Comparison of accuracy (%) under few-shot learning settings on the FluoMix mouse brain dataset. CoOp follows the experimental protocol from the original paper [23], using prompt tuning only. CoOp+ E_{img} extends CoOp by additionally fine-tuning the image encoder together with the prompts. OrdinalCLIP and FluoCLIP follow the main ResNet-50 experiment configuration described in Sec. 6. FluoCLIP exhibits the **steepest** improvement curve as supervision increases, demonstrating a strong stain-aware prior that enables rapid adaptation in low-data regimes. Results are reported as mean \pm standard deviation over five runs with different random seeds.

#-Shots	1	8	16	32	64	128
CoOp [23]	11.72 \pm 1.10	16.32 \pm 0.91	17.88 \pm 0.44	18.36 \pm 0.61	18.38 \pm 0.44	18.50 \pm 0.50
CoOp+ E_{img} [23]	13.58 \pm 1.88	14.92 \pm 1.10	14.98 \pm 0.88	15.82 \pm 1.17	17.06 \pm 0.78	19.22 \pm 1.17
OrdinalCLIP [13]	15.51 \pm 1.15	19.43 \pm 0.98	19.55 \pm 0.29	20.60 \pm 0.91	21.18 \pm 0.50	19.99 \pm 2.06
FluoCLIP	11.69 \pm 1.15	15.92 \pm 0.89	18.90 \pm 1.32	20.45 \pm 0.87	24.41 \pm 0.52	29.11\pm2.13

Table 11. Comparison of accuracy (%) results under few-shot settings on a held-out fluorescence microscopy dataset acquired from **mouse lung tissue** with a **known staining combination** (Alexa 488, Cy3, and Alexa 647). We observe that from the 32-shot regime, FluoCLIP exhibits a clear advantage, suggesting that its stain-aware modeling begins to effectively leverage **stain-specific signal variation** when sufficient examples are available. The results are mean \pm standard deviation over five random seeds.

#-Shots	1	8	16	32	64	128
OrdinalCLIP [13]	20.09 \pm 0.42	21.87 \pm 1.23	23.99 \pm 0.50	29.14 \pm 0.66	41.26 \pm 1.01	61.73 \pm 0.62
FluoCLIP	20.35 \pm 0.79	20.95 \pm 1.05	23.51 \pm 0.62	29.43 \pm 0.63	43.27 \pm 1.19	67.97 \pm 1.31

Table 12. Comparison of accuracy (%) under few-shot settings on held-out fluorescence microscopy datasets of unseen **mouse lung, liver** tissues with an unseen staining combination (Hoechst 33342 and DAPI). Because both stains target the nucleus and are visually similar to Hoechst 34580 used during base training, OrdinalCLIP performs better in the extremely low-shot regime. However, from the 32-shot setting onward, FluoCLIP shows a clear advantage, demonstrating its ability to leverage **stain-aware adaptation** once sufficient examples become available. The results are reported as mean \pm standard deviation over five random seeds.

#-Shots	1	8	16	32	64	128
OrdinalCLIP [13]	19.82 \pm 1.85	25.36 \pm 1.23	29.37 \pm 0.68	34.46 \pm 1.25	42.82 \pm 0.74	54.35 \pm 1.17
FluoCLIP	18.75 \pm 2.04	24.54 \pm 0.93	29.20 \pm 1.00	34.90 \pm 1.45	44.57 \pm 1.18	57.71 \pm 0.46

11.2. Few-Shot Generalization to Unseen Tissues

Next, we evaluated FluoCLIP along the *tissue generalization* axis by testing its ability to adapt to previously unseen tissues while keeping the stain conditions fixed. The model was pretrained on brain tissue (D1–D4) and then adapted using k labeled samples per focus rank per stain from lung-tissue images (D5) stained with Alexa 488, Cy3, and Alexa 647. For this setting, the few-shot training set is constructed using the same sampling protocol— k labeled samples per focus rank for each stain ($k = \{1, 8, 16, 32, 64, 128\}$)—resulting in $3 \times 10 \times k$ training samples.

Tissue-dependent variations introduce substantial domain shifts in cellular morphology, density, and spatial texture, making this setting more challenging. As shown in Table 11, OrdinalCLIP [13] performs slightly better in the

lowest-shot regime due to its stain-agnostic design, which avoids committing to stain priors that may behave differently across tissues. However, FluoCLIP again shows a sharp performance increase as k grows, surpassing OrdinalCLIP from the 32-shot regime onward. This indicates that FluoCLIP’s stain-grounded modeling generalizes effectively across tissue-dependent fluorescence variations once modest supervision becomes available.

11.3. Few-Shot Generalization to Unseen Stain & Tissue Pairs

We now evaluate the most challenging generalization setting, where both the stain and the tissue differ from those seen during base training. Starting from a checkpoint trained on the FluoMix brain-tissue subset (D1–D4), we adapt the model to two entirely unseen nuclear stains—

Hoechst 33342 (D5–D6) and DAPI (D7)—each acquired from different tissues than the training domain. Adaptation uses only k labeled samples per focus rank for each stain ($k = \{1, 8, 16, 32, 64, 128\}$), resulting in $2 \times 10 \times k$ training images.

To ensure comparability with earlier experiments, we restrict evaluation to nucleus-targeting stains (DAPI, Hoechst 33342). Since these stains highlights the same biological structure, morphological differences caused by tissue variability are reduced, allowing stain-dependent optical differences to be examined more clearly (Fig. 5)

As shown in Table 12, OrdinalCLIP [13] slightly outperforms FluoCLIP at 1–16 shots. Because all unseen stains in this setting target the nucleus and therefore appear visually similar to Hoechst 34580 stained images from the base training domain, OrdinalCLIP’s stain-agnostic prompts generalize reasonably well in this extremely low-shot regime. In contrast, FluoCLIP has insufficient samples to learn the subtle stain-specific variations. However, as more labeled samples become available, FluoCLIP quickly surpasses all baselines and widens the performance gap at 32–128 shot range. This demonstrates that explicit stain grounding provides superior adaptability when both the stain and tissue shift simultaneously, becoming increasingly advantageous once even modest supervision is available.

12. Ablation Study

To understand the contribution of each component in FluoCLIP, we conduct a systematic ablation by varying the stain-token type, the use of the two-stage grounding pipeline, and the inclusion of the text-side adapter.

We compare three types of stain tokens: S^{plain} is a non-learnable text token that simply inserts the stain name, S^{train} is a learnable token updated during training without explicit grounding, and S is our grounded stain token obtained through the two-stage procedure.

Table 13 varies two factors that jointly define the stain-token type—Fine-tune(S) (trainable vs. frozen tokens) and Two Stage (with vs. without stain grounding)—along with an additional orthogonal choice of whether to include the text-side Adapter after CLIP text encoder.

With this ablation, we evaluate how different learning strategies for stain tokens—from frozen tokens to naïve trainable tokens to grounded tokens—and the presence of adapter affect the model’s ability to acquire robust stain-aware focus representations.

Effects of Stain-Grounding. Configuration (A) uses non-learnable stain tokens (S^{plain}), while (C) replaces it with learnable stain tokens (S^{train}) but without the grounding stage (Two Stages). Interestingly, (C) performs worse than (A), indicating that simply making stain tokens trainable does not help. Without the grounding phase, the model re-

Table 13. Ablation of FluoCLIP’s learning strategy. We evaluate how stain tokens should be trained and whether the text-side adapter provides additional gains. Configuration (A-F) combines three stain-token variants (S^{plain} : frozen, S^{train} : naively trained, S : grounded via two-stage learning) with optional use of the grounding pipeline (Two Stages) and the adapter (Adapter). Results (mean \pm std over five seeds) isolate the contribution of stain grounding, trainability, and adapter design.

Type	Configuration	Fine-tune (S)	Two Stage	Adapter	Accuracy (%) \uparrow
(A)	S^{plain}	×	×	×	81.04 \pm 0.81
(B)	S^{plain} + Adapter	×	×	o	83.21 \pm 3.93
(C)	S^{train}	o	×	×	80.50 \pm 0.67
(D)	S^{train} + Adapter	o	×	o	81.38 \pm 0.63
(E)	S	o	o	×	81.83 \pm 0.95
(F)	S + Adapter	o	o	o	84.28 \pm 0.88

ceives no visual constraint linking stain-specific text features to fluorescence appearance, and learning tends to inject noise rather than meaningful stain semantics.

When the grounding phase is enabled (E), the performance increases over both (A) and (C) (by +0.79% and +1.33%, respectively), demonstrating that explicit grounding is essential for producing stain tokens that actually reflect stain-dependent optical cues. Importantly, these gains appear even before introducing the adapter, confirming that grounding—not trainability alone—is the key factor.

Effects of Adapter. Configuration (B) and (D) evaluate the adapter with non-grounded stain tokens (S^{plain} in (B), S^{train} in (D)). The adapter yields moderate improvements in both cases, but the gains remain limited because the underlying stain tokens are not aligned with visual features. Thus, architectural augmentation alone cannot produce meaningful stain-aware embeddings—the adapter benefits only materialize when the stain tokens themselves are grounded.

Combined Effects. Configuration (E) and (F) corresponds to the two-stage FluoCLIP pipeline, with (F) additionally using the text-side adapter. Grounded stain tokens alone (E) already outperform all non-grounded alternatives (A, C), verifying that the grounding stage is the primary source of performance improvement. Adding the adapter (F) achieves the best results overall (84.28%), confirming that grounded stain semantics and the adapter contribute complementary benefits. Overall, these ablations demonstrate that (i) stain-grounding is necessary for producing stable and informative stain-aware embeddings, and (ii) the adapter further refines these representations, but works best when grounding is present. This explains why the full FluoCLIP pipeline achieves the strongest performance.

Algorithm 1 Overall Workflow of FluoCLIP

Stage 1: Stain-Grounding**Input (Stage 1):**

Training set $\mathcal{D}_{\text{stain}} = \{(x_i, s_i)\}$
Stain tokens \mathbf{S} , adapter \mathcal{A}
Context tokens $C = \{[stain-context]\}$
Image encoder E_{img}
Text encoder E_{text}

Output (Stage 1):

Updated \mathbf{S}, \mathcal{A}

- 1: **for** epoch = 1 to stage1_max_epoch **do**
- 2: Generate Prompt $\mathcal{P}^{\text{stain}}$ (Eq. 3)
- 3: **for** $(x_i, s_i) \in \mathcal{D}_{\text{stain}}$ **do**
- 4: Encode Image $v_i \leftarrow E_{\text{img}}(x_i)$
- 5: Encode Text $t_l^{\text{stain}} \leftarrow \mathcal{A}(E_{\text{text}}(\mathcal{P}^{\text{stain}}))$
- 6: Calculate Similarity $z_{i,l}^{\text{stain}} = \langle v_i, t_l^{\text{stain}} \rangle$
- 7: Update \mathbf{S}, \mathcal{A}
- 8: **end for**
- 9: **end for**

Stage 2: Stain-Guided Ranking**Input (Stage 2):**

Training set $\mathcal{D}_{\text{rank}} = \{(x_i, s_i, r_i)\}$
Grounded stain tokens \mathbf{S} , adapter \mathcal{A} from Stage 1
Base ranks \mathbf{R}^{base}
Conditioning network f_θ
Context tokens $C = \{[stain-context], [rank-context]\}$

Output (Stage 2):

Updated $\mathbf{R}^{\text{base}}, f_\theta, E_{\text{img}}, C$

- 10: **for** epoch = 1 to stage2_max_epoch **do**
 - 11: Generate Stain-Guided Rank $\tilde{\mathbf{R}}_k^l$ (Eq. 5, 6)
 - 12: **for** $(x_i, s_i, r_i) \in \mathcal{D}_{\text{rank}}$ **do**
 - 13: Encode Image $v_i \leftarrow E_{\text{img}}(x_i)$
 - 14: Generate Prompt $\mathcal{P}^{\text{rank},i}$ (Eq. 7)
 - 15: Encode Text $t_k^{\text{rank},i} \leftarrow \mathcal{A}(E_{\text{text}}(\mathcal{P}^{\text{rank},i}))$
 - 16: Calculate Similarity $z_k^{\text{rank},i} = \langle v_i, t_k^{\text{rank},i} \rangle$
 - 17: Update $\mathbf{R}^{\text{base}}, f_\theta, E_{\text{img}}, C$
 - 18: **end for**
 - 19: **end for**
-

kens, are assembled into sample-specific sentences and encoded by the frozen CLIP text encoder. Image–text similarities are then used to predict the focus rank, while the base rank tokens, context tokens, conditioning network, and image encoder are updated with ranking supervision.

13. Algorithm

Algorithm 1 outlines the overall two-stage pipeline of FluoCLIP. **Stage 1** performs *stain-grounding*, in which the stain tokens and adapter are optimized with stain-class supervision to align vision–language representations with fluorescence-specific stain semantics. **Stage 2** conducts *stain-guided ranking*. The grounded stain embeddings modulate the base rank embeddings through a conditioning network, and interpolation yields continuous stain-conditioned rank tokens. These rank tokens, together with learnable context tokens and the fixed grounded stain to-

Table 14. Ablation study on FluoCLIP components on the FluoMix dataset. The baseline (OrdinalCLIP [13]) includes only the focus token. We incrementally add grounded stain tokens (D) and stain-guided rank modules (E) to evaluate their individual contributions.

Type	Configuration	S^{plain}	S^{train}	S	R	\tilde{R}^S	Acc. (%)
(A)	Baseline (OrdinalCLIP) with Rank (R)			✓	✓		83.12±0.41
(B)	(A) + Plain Stain Token (S^{plain})	✓			✓		83.21±3.93
(C)	(A) + Learnable Stain Token (S^{train})		✓		✓		81.38±0.63
(D)	(A) + Grounded Stain Token (S)			✓	✓		84.28±0.88
(E)	(D) + Stain-Guided Rank Token			✓		✓	85.21±0.88